Mechanics & Industry **26**, 9 (2025)

https://doi.org/10.1051/meca/2025002

Mechanics & Industry

Available online at:
www.mechanics-industry.org

ORIGINAL ARTICLE OPEN ACCESS

Parametric-modeling-based multi-objective thermoelastic optimization of rudder structures

Guanghui Shi[1,2], Yuhao Bao[1], Wenhua Wu[1], Guiqiang Guo[2], Ye Lin[2], Xiaopeng Zhang[1,*], and Ran Tao[3,*]

[1] State Key Laboratory of Structural Analysis, Optimization and CAE Software for Industrial Equipment, Dalian University of Technology, Dalian 116024, China
[2] Structural Design and Strength Technology Research Center, Beijing Electro-Mechanical Engineering Institute, Beijing 100074, China
[3] Institute of Advanced Structure Technology, Beijing Institute of Technology, Beijing 100081, China

Received: 9 March 2024 / Accepted: 13 January 2025

Abstract. Lightweight optimization of rudder structures subjected to thermo-mechanical coupling is essential for high-speed aircraft but poses significant challenges. Therefore, this paper proposes an enhanced multi-objective thermoelastic optimization method for rudder structures. The improvements involve the inclusion of thermal effects to enhance adaptability to extreme thermal environments, refining the optimization strategy to achieve clear resulting structural configurations, parametric optimization variables enabling combined optimization of parameters and configurations, and incorporating dynamic response constraints to ensure key dynamic responses meet usage requirements. To efficiently analyze and optimize the structural performance of rudder structures, a parametric optimization model for the radial configuration of reinforcement ribs is constructed. The objective of the optimization is to reduce the weight of the rudder structure while considering both frequency and maximum displacement indicators by formulating a multi-objective normalized objective function. These optimization problems are solved using a compromise programming algorithm. The proposed optimization method reduces the weight of the rudder structure by 21.2% while meeting the design indicators under service conditions. The obtained optimization parameters can guide the detailed modeling of the rudder structure, and the optimization results have been further verified through finite element analysis. By leveraging commercial software and established optimization algorithms, this method can be adapted to other thermoelastic optimization challenges through refinements such as parametric modeling and multi-objective optimization functions. And this method is particularly suitable for the thermo-mechanical coupled optimization design of aircraft rudder structures.

Keywords: Multi-objective optimization / aircraft rudder / thermoelastic optimization / parametric modeling

1 Introduction

In high-speed vehicles, such as aircraft and high-performance racing cars, control surfaces like rudders, ailerons, and elevators are subjected to both aerodynamic pressure and thermal loads [1,2]. The aircraft's rudder structure, a quintessential load-bearing component, functions dually as a lifting element and as a critical control mechanism for the aircraft's pitch and yaw maneuvers. The weight of the complete structure directly impacts the power consumed by the actuator and electrical energy usage, thereby affecting the spatial utilization and payload capacity of the aircraft. Reducing the mass of the rudder structure can shift the center of gravity of the aircraft forward, thereby improving the overall control characteristics and lowering the aircraft weight [3]. Furthermore, adjusting the frequency characteristics of the control surface structure can help mitigate aeroelastic issues, such as flutter [4,5]. Under the complex conditions of severe force loads and intense aerodynamic heating, the static and dynamic aeroelastic design of rudder structures are essential yet remains a challenging task [6,7]. Consequently, it is necessary to develop an effective and efficient design optimization method for rudder structures.

In general, primary considerations encompass the geometric configuration, dimensional specifications, and material distribution within the structural framework. The optimization process involves applying mathematical algorithms and engineering principles [8]. Various optimization-based design methods have been established for designing a range of aerospace structures, such as aircraft

* e-mails: zhangxiaopeng@dlut.edu.cn; taoran@bit.edu.cn

wings [9–12], stiffener ribs [13–15], multi-fasteners [16–18], and multi-component structure systems [19–21]. Moreover, extensive research efforts have been dedicated to achieving lightweight designs and enhancing the key performance indicators of rudder structures through various optimization strategies [22–25].

Notably, most existing studies on the design and optimization of rudder structures combine topology optimization with parameter optimization to significantly enhance traditional configurations. In such methods [26–28], the first step is to conduct rudder topology optimization to determine the optimized rib topology configuration. Subsequently, model reconstruction is performed to derive a parametric optimization design model. Specifically, without altering the topology of the reinforcing ribs, parameter optimization is conducted, including design variables such as rib thickness and skin thickness. This process yields the structural parameters that can guide structural design. For example, Zhu drew inspiration from the multi-level fish-gill bone structure typically used in wing-like structures and introduced biomimetic principles into the optimization design of aircraft rudder structures to establish a feature-driven topology optimization method that integrates the structural layout and size parameters [23]. Song performed the thermal-elastic topology optimization of additively manufactured rudders, considering both mechanical and thermal loads [25]. Notably, a key challenge in the optimization of rudder structures is that the topology optimization of load-bearing structures, when accounting for thermal stress, tends to yield numerous small and weak rib reinforcement structures. This results in unclear topology configurations and increases the complexity of model reconstruction. Although existing topology optimization methods for rudder structures can help clarify rib configurations that meet performance criteria, certain limitations remain, such as the prolonged design process, information loss during the transition from topology optimization to parameter optimization, and incompatibility with traditional machining manufacturing methods.

The optimization of rudder surface parameters and configurations within the aerospace domain necessitates a design process that integrates mechanical performance criteria, multidisciplinary requirements, and is attentive to the constraints imposed by manufacturing processes. In the initial design stage, multidisciplinary optimization can be conducted with aerodynamic performance considerations. Subsequently, parametric optimization can be directly performed during the detailed design stage. For example, Haftka integrated the lift-line aerodynamic model with a structural finite element model, thereby introducing the concept of optimizing aerodynamic performance and structural response under flight conditions [8]. Rao devised a program aimed at the parametric optimization design of wing structures, through which he optimized wing structure parameters under diverse operational scenarios [29]. In recent years, there has been a growing trend towards considering composite material wing structures and their design under aerodynamic loads [30,31]. This shift has facilitated the gradual development of multidisciplinary optimization platforms [32], which have found application in the conceptual and preliminary design phases of aircraft [12].

The joint optimization of aerodynamics and structure for wing surfaces, as well as the topology optimization of rudder structures, have yielded promising results. However, there is still room for expanding the range of design variables and improving the efficiency of structural optimization in rudder load-bearing structures, an area that scholars continue to explore. Hu introduced a method for the full parameter optimization design of wing components based on segmented polynomial expressions and a global optimization algorithm [33]. This method reduces the number of optimization variables, thereby enabling simpler and more efficient optimization.

This paper presents a multi-objective thermal-elastic optimization design method for rudder structures, utilizing fully parametric geometry and finite element modeling. The primary goal is to enhance the optimization efficiency for rudders under the combined influence of force and thermal loads, resulting in a model that meets design requirements and can be directly utilized for manufacturing. To achieve this, a parametric modeling strategy driven by finite alterations in reinforcement ribs is established, based on traditional rudder configurations. This model considers both the number of radial reinforcement ribs and multiple dimensional parameters that significantly impact structural performance. The full parametrization modeling technique enables automated modeling and finite element analysis of intricate structures, thereby simplifying the structural optimization process. In tackling the complex, multi-objective, and nonlinear structural response optimization problem, which inherently involves coupled variables, this study employs an intelligent optimization approach grounded in the principles of compromise programming. This method generates optimized designs with radial reinforcement topology and optimized dimensional parameters. Additionally, the impact of different temperature fields on the optimized structural configurations and detailed parameters is investigated through various numerical examples.

The remaining paper is structured as follows: Section 2 introduces the initial rudder structure model and its key parameter responses, which serve as a comparison benchmark for further optimization. Section 3 describes the theoretical model, including the thermo-mechanical coupling calculation model and the compromise programming multi-objective optimization design model. Section 4 discusses the optimized rudder structures and corresponding key parameters under various temperature fields, and outlines the findings from a regularity analysis. Section 5 presents the concluding remarks.

2 Analytical model of rudder structure

2.1 Model description

The object of interest is a fully movable rudder structure on an aircraft, as illustrated in Figure 1. In general, rudders are located at the rear of the aircraft, typically protruding from its surface, and are arranged in a "+" or "×" shape.

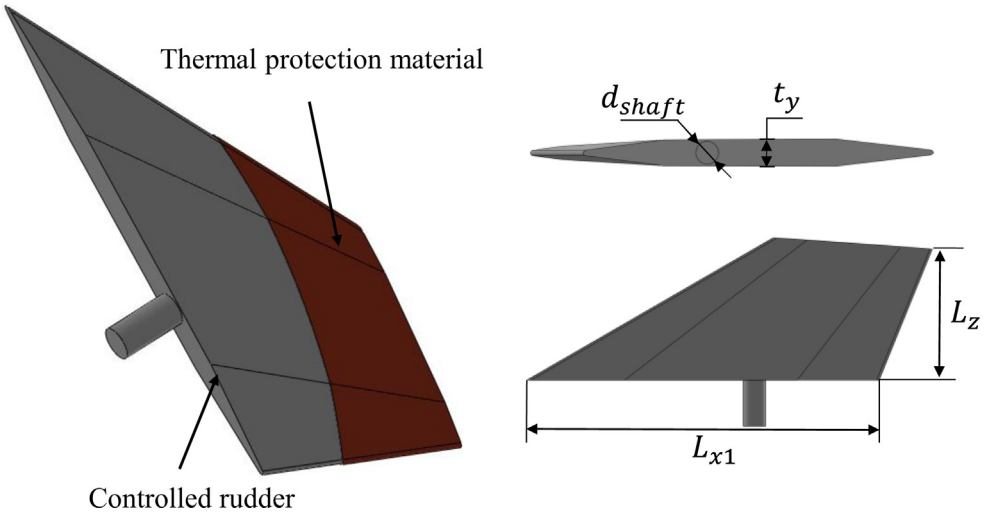

Fig. 1. Aerodynamic shape of the rudder structure.

During operation, according to the flight plan design, the onboard control system actuates the rudder to produce different deflection angles, facilitating pitch and lateral maneuvers. Simultaneously, the rudder generates lift to balance the aircraft's weight. The rudder's aerodynamic cross-sectional profile is designed with a shuttle-like geometry, featuring a tapered shape at both the leading and trailing edges to optimize drag reduction. Generally, the rudder surface of high-speed aircraft is covered with thermal insulation materials, such as high-temperature resistant coatings or other thermal protection materials.

This research rudder has the following primary dimensions: maximum size in the x-direction (chord direction), L_x, of 710 mm; maximum envelope size in the z-direction (span direction), L_z, of 330 mm; maximum size in the y-direction (thickness), t_y, of 50 mm; and diameter of the rudder shaft, d_{shaft}, of 40 mm, as shown in Figure 1.

2.2 Finite element solution of the thermo-mechanical coupling problem

For the thermo-mechanical coupling analysis of the rudder structure, the thermo-mechanical equilibrium equation can be expressed as follows:

$$\begin{cases} -\mathrm{div}(\sigma) = f \ \ \mathrm{in}(0,t_f) \times D, \\ \sigma = \sigma^{\mathrm{el}} - \sigma^{\mathrm{th}} \ \ \mathrm{in}(0,t_f) \times D, \\ \sigma^{\mathrm{el}} = \mathbf{D}e(u) \quad \sigma^{\mathrm{th}} = \mathbf{D}\varepsilon^{\mathrm{th}}\varepsilon^{\mathrm{th}} = \alpha(T - T_{\mathrm{init}})\mathrm{I}_n, \\ \sigma \cdot n = 0 \quad \mathrm{on}(0,t_f) \times \partial D_N, \\ u = 0 \quad \mathrm{on}(0,t_f) \times \partial D_D, \end{cases} \tag{1}$$

where $\boldsymbol{D}$ is the spatial domain where the problem is analyzed; ∂D_N represents the Neumann boundary; ∂D_D denotes the Dirichlet boundary; $\boldsymbol{\sigma}$ is the Cauchy stress tensor, decomposed as the sum of the elastic stress $\boldsymbol{\sigma}^{\mathrm{el}}$ and thermal stress $\boldsymbol{\sigma}^{\mathrm{th}}$; $\boldsymbol{\varepsilon}^{\mathrm{th}}$ means the thermal strain; $\boldsymbol{D}$ is the fourth-order elasticity tensor of an isotropic material with Young's modulus $E > 0$ and Poisson ratio $-1 < \nu < 1/2$; I_n is the identity matrix; α is the thermal expansion coefficient. The finite element form of equation (1) is as follows:

$$\mathbf{KU} = \mathbf{F}^{\mathrm{el}} + \mathbf{F}^{\mathrm{th}}, \tag{2}$$

where $\boldsymbol{K}$ is the global element stiffness matrix, $\boldsymbol{F}^{\mathrm{el}}$ is the external force load vector, and $\boldsymbol{F}^{\mathrm{th}}$ is the equivalent thermal force load. The global stiffness matrix of the structure is assembled from the element stiffness matrix $\boldsymbol{K_e}$ of each element, and the thermal stress load vector $\boldsymbol{F}^{\mathrm{th}}$ is assembled from the element thermal force $\boldsymbol{F}_{\boldsymbol{e}}^{\mathrm{th}}$ of each element. The element stiffness Ke and thermal force $\boldsymbol{F}_{\boldsymbol{e}}^{\mathrm{th}}$ can be represented in the following form:

$$\begin{cases} \mathbf{K}_e = \int_{V_\mathbf{e}} \mathbf{B}_e^T \mathbf{D}_e \mathbf{B}_e dV \\ \mathbf{F}_e^{\mathrm{th}} = \int_{V_\mathbf{e}} \mathbf{B}_e^T \mathbf{D}_e \varepsilon_e^{\mathrm{th}} dV \end{cases}, \tag{3}$$

where the element strain-displacement matrix, $\boldsymbol{B_e}$, is composed of the derivatives of the element shape functions [34].

3 Optimization model and algorithm

3.1 Design variables and parametric modeling

Considering empirical design principles, the internal rib structure of the reference rudder features a classic configuration with radial and circumferential ribs. This reinforcement structure enables force transmission from the rudder load to the rudder shaft constraint end, ensuring high force transmission efficiency and overall comprehensive performance. Therefore, this radial rib design is commonly used in aircraft [35,36], with variations in the number, position, and thickness parameters of the radial ribs based on design indicators such as rudder size, service load environment, and functional constraints (e.g., weight, center of gravity, frequency, and maximum deformation).

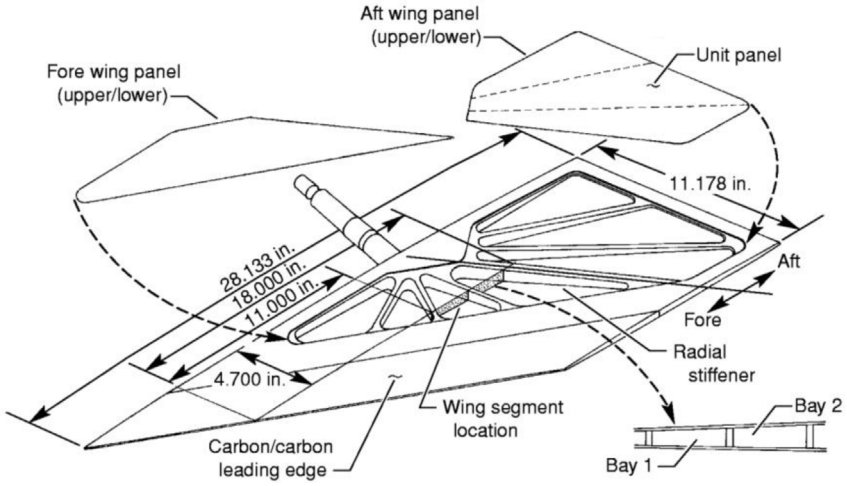

Fig. 2. Classical rudder structure A [35].

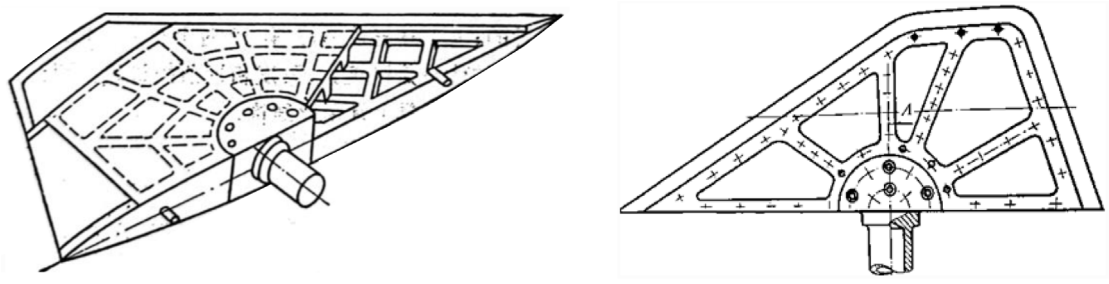

Fig. 3. Classical rudder structure B and C [36].

The optimization process of the rudder structure begins with a classic rudder structure configuration that satisfies the design indicators at room temperature (20°C). This type of radial ribbed rudder structure is a classic configuration that is widely used on various aircraft, as shown in Figures 2 and 3.

In this research, a parametric model of the radial rib structure is constructed, considering variables such as the number of radial ribs, rib thickness, rudder skin parameters, bottom rib thickness, and top rib thickness. This process entails detailed parameterization of the reinforced rudder configuration. This methodology's distinct advantage lies in its ability to amalgamate established rudder design principles with a flexible adaptation mechanism to accommodate diverse performance indices, tailored to meet specific dynamic and thermal loading conditions. Specifically, this approach optimizes the radial rib distribution and their detailed parameters, yielding an engineering rudder structure configuration that can be used for direct structural modeling.

Based on the classic design [35,36], the rudder structure design parameters are simplified, as shown in Figure 4. The design variables are $X=[x_1, \ldots, x_7]^T$, including two categories: structural thickness parameters $x_1 \sim x_6$ and the number of radial ribs x_7. This optimization problem includes seven design variables, and challenges may arise during the modeling process due to the interdependence and interference among various geometric parameters. Modifying these parameters may result in failures of geometric modeling or the creation of excessively intricate meshes, thereby hindering subsequent analytical and optimization processes. Therefore, full-parameterization modeling is essential for the considered problem. The parametric modeling process mainly involves five steps, as shown in Figure 5.

Step 1: Construct a parametric model for the radial ribs. The design variables of a single radial rib include the thickness x_6 and the quantity x_7. With the intersection point of the rudder axis and bottom of the rudder set as the center, x_7 radial ribs are arranged radially across the rudder surface. In this stage, the radial rib structure does not conform to the aerodynamic shape of the rudder and extends beyond its surface.

Step 2: The regular radial rib structure is integrated with the pre-modeled ring rib structure, resulting in a regular reinforcement rib set.

Step 3: The regular reinforcement rib set intersects with the aerodynamic shape of the pre-modeled rudder body, yielding an irregular reinforcement rib set that aligns with the rudder's aerodynamic shape.

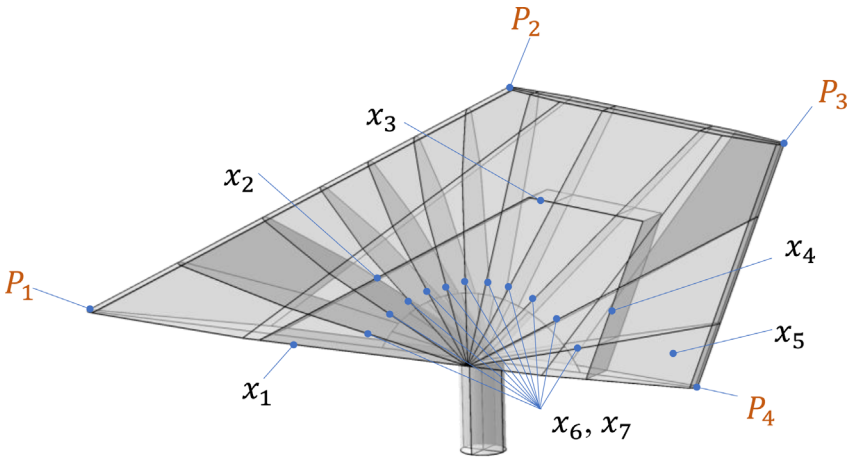

Fig. 4. Rudder structure design parameters.

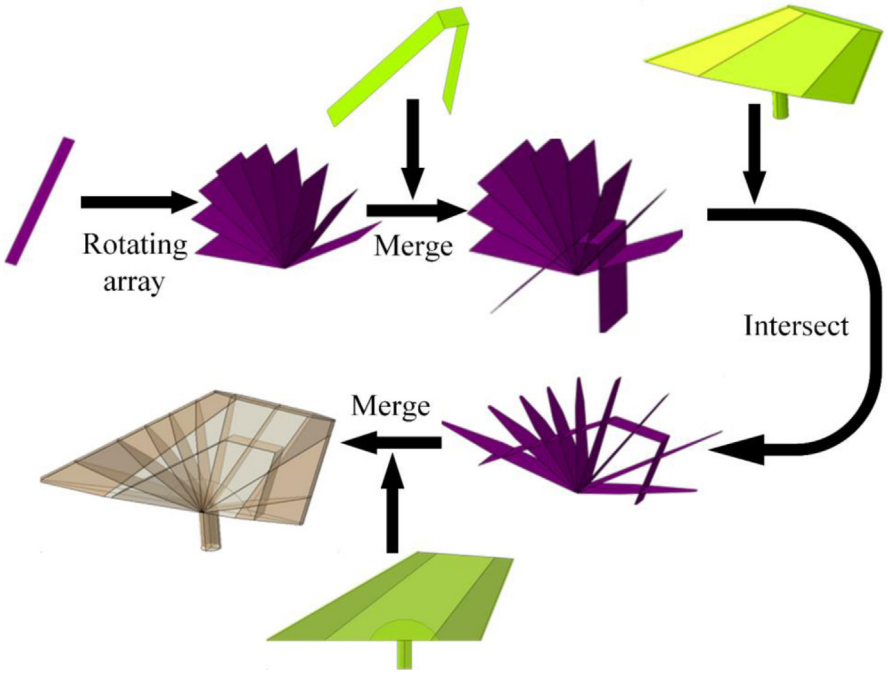

Fig. 5. Process flow of parametric modelling.

Step 4: The irregular reinforcement rib set is combined with the pre-modeled outer skin and rudder axis position structure, thereby yielding the complete thin-walled rudder structure incorporating the internal reinforcement ribs. At this stage, the parametric modeling of the load-bearing structure of the rudder is completed.

Step 5: The design variables are assigned to the thickness parameters at different positions of the rudder structure. Subsequently, the finite element boundary conditions, force loads, temperature loads, and other parameters are updated based on the new model. This marks the completion of the finite element parametric modeling.

The following assumptions are incorporated into parametric modeling. First, as the primary objective of this research is to optimize the number of radial rib configurations and detailed structural parameters while preserving the existing configuration, all parameters are assigned a range of values during the parametric modeling phase based on engineering experience. Second, to ensure manufacturing feasibility, the minimum increment for structural parameters is set to 0.1mm. Based on these assumptions, along with engineering experience and insights from numerous test cases, efforts are made to avoid both an overly expansive design space, which may result in prolonged iteration periods, and an extremely constrained design space, which may impede the discovery of the optimized solution. The design space for each design variable is detailed in Table 1.

3.2 Multi-objective optimization based on compromise programming

In the design and optimization of the rudder structure, key considerations include the rudder weight, maximum displacement, and total elastic strain energy. Therefore,

Table 1. Design variables and corresponding geometric features.

Design variables	Geometric features	Relationship and design space
x_1	Bottom and top thickness t_1	$t_1 = 0.5 + 0.1 \times x_1(\text{mm})$, $t_1 \in [0.5, 10]$
x_2	Top ring rib thickness t_2	$t_2 = 0.5 + 0.1 \times x_2(\text{mm})$, $t_2 \in [0.5, 5]$
x_3	Left ring rib thickness t_3	$t_3 = 0.5 + 0.1 \times x_3(\text{mm})$, $t_3 \in [0.5, 5]$
x_4	Right ring rib thickness t_4	$t_4 = 0.5 + 0.1 \times x_4(\text{mm})$, $t_4 \in [0.5, 5]$
x_5	Outer panel skin thickness t_5	$t_5 = 0.5 + 0.1 \times x_5(\text{mm})$, $t_5 \in [0.5, 5]$
x_6	Radial rib thickness t_6	$t_6 = 0.5 + 0.1 \times x_6(\text{mm})$, $t_6 \in [0.5, 5]$
x_7	Number of radial ribs n_{rb}	$n_{\text{rb}} = x_7$, $n_{\text{rb}} \in [2, 10]$

the optimization problem considered in this study is a typical multi-objective optimization problem. The general form of this problem can be expressed as follows:

$$\begin{cases} min(\{f_1(x), f_2(x), \cdots, f_k(x)\}) \\ s.t.\ x \in X \end{cases}, \tag{4}$$

where $f_i(x)$ is the sub-objective function. The constraint $x \in X$ refers to $x \in X = \{x \in R^n | g_j(x) \leq 0\,; h_l(x) = 0\}$, where $g_j(x) \leq 0$ and $h_l(x) = 0$ are the inequality and equality constraints, respectively.

In scenarios where sub-objective functions are devoid of conflicts, an optimized solution can be readily derived using a weighted approach. Nevertheless, the reality is that numerous sub-objectives often interact with one another, manifesting in either synergistic or antagonistic relationships. In the presence of two or more conflicting sub-objective functions, the improvement in one function toward the optimized solution may result in the opposite deviation of another function from its optimal solution. Consequently, simple weighting cannot be applied to normalize multiple objectives, especially in multi-parameter non-convex programming problems. Moreover, objective functions with different dimensions necessitate careful normalization. A more effective method is to convert the absolute distance between the compromise solution and the ideal solution for each sub-objective function into relative distances, thereby facilitating their comparison. Additionally, the compromise programming approach, which is well-suited for multi-objective problems, is used in this study [37–41]. Consequently, the multi-objective function is transformed into a unified single-objective function problem. A single sub-objective after normalization takes the following form:

$$f_{ni}(\mathbf{x}) = \frac{f_i(\mathbf{x}) - f_{min}}{f_{\max} - f_{min}}, \tag{5}$$

where $f_{ni}(x)$ is the normalized objective function, $f_i(x)$ is the objective function before normalization, f_{max} is the value of the worst solution and f_{min} is the value of the best solution. Therefore, the normalized comprehensive objective function can be expressed as:

$$min\left\{ \left[\sum_{i=1}^{k} \lambda_i^p \left(\frac{f_i(\mathbf{x}) - f_{min}}{f_{\max} - f_{min}} \right)^p \right]^{1/p} \right\}, \tag{6}$$

where λ_i^p is the weight value of the i-th objective function; and p is the penalty factor, satisfying $1 \leq p < \infty$.

For this rudder structure optimization problem, the objective is a combination of the structure weight, maximum displacement, and total elastic strain energy. A penalty factor $p = 2$ is selected with the rationale that this parameterization enhances the efficiency of the optimization process, particularly in the early stages of the objective function's search phase [42–44]. And this makes the normalized comprehensive objective function represents the Euclidean distance between two points in physics. Then, the comprehensive objective function in i-th step can be established as:

$$f_i = \sqrt{\begin{array}{c} \left(\lambda_1 \frac{C_i - C_{min}}{C_{\max} - C_{min}}\right)^2 + \left(\lambda_2 \frac{M_i - M_{min}}{M_{\max} - M_{min}}\right)^2 \\ + \left(\lambda_3 \frac{U_i - U_{min}}{U_{\max} - U_{min}}\right)^2, \end{array}} \tag{7}$$

where f_i is the comprehensive objective function in i-th step; λ_1, λ_2, λ_3 are the weight coefficients of strain energy, mass, and maximum displacement in the objective function, respectively; C_i, M_i, U_i represent the strain energy, structural weight, and maximum deformation of the structure in i-th iterative solution. The normalization of three single-objective functions is involved, which are the structural strain energy, structural weight, and structural self-large deformation, represented by C, M, U respectively. C_{max}, M_{max}, U_{max}, C_{min}, $M_{\min}$, $U_{\min}$ are pre-solved before the optimization iteration, obtained through finite element method solutions. C_{mim}, M_{max}, U_{min} correspond to the upper limits of the design variables. Correspondingly, C_{max}, M_{min}, U_{max} correspond to the lower limits of the design variables.

The objective is to minimize the normalized comprehensive objective function f, subject to the constraint of a minimum fundamental frequency for the rudder structure. This frequency is determined based on the initial structure model. Therefore, the optimization problem can be formulated as follows:

$$\begin{aligned} &\text{find}: \mathrm{X} = \{x_i\}, i = 1, 2, \cdots, k \\ &\min: f \\ &\text{s.t.}: \mathbf{KU} = \mathbf{F}^{\text{el}} + \mathbf{F}^{\text{th}} \\ &\qquad \omega > \omega_0 \\ &\qquad \mathbf{0} < x_{\text{low}} \leq \mathrm{x} \leq \mathrm{x}_{\text{up}}. \end{aligned} \tag{8}$$

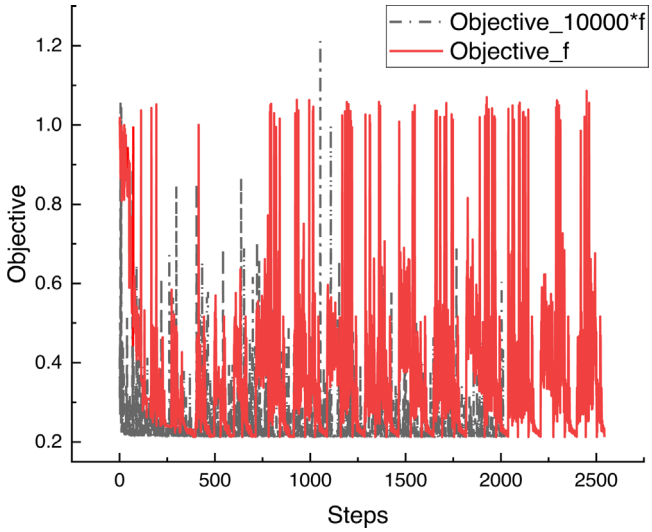

Fig. 6. Test examples with different objective.

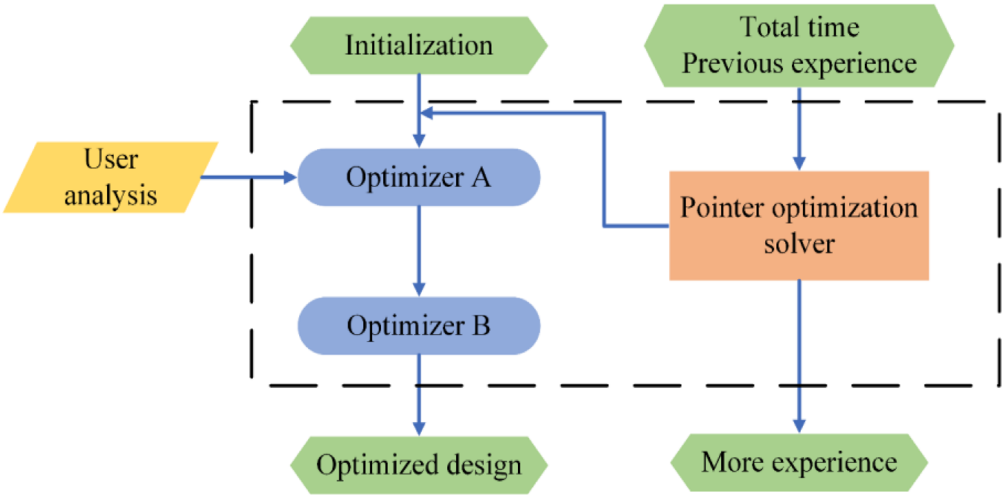

Fig. 7. Internal control strategy of pointer automatic optimizer.

Post-normalization, the values of the sub-objective functions lie within a small range of 0 and $\sqrt{3}$. To prevent the algorithm from being affected by truncation errors in significant digits during iterative optimization, the objective function is magnified by 10,000 times during the optimization iteration. And testing examples have shown that, when using the initial structural parameters as the starting values, and respectively adopting f and 10000*f as the objective functions for iteration, the example with 10000*f as the objective function achieves higher convergence efficiency. The iterative convergence process is shown in Figure 6.

The optimization problem is solved using the Pointer Automatic Optimizer [45], which consists of a complementary set of optimization algorithms. The Pointer technique can efficiently solve a wide range of problems in a fully automatic manner due to a special automatic control algorithm, making it especially suitable for non-smooth continuous optimization problems [46–48]. Its main disadvantage is the longer iteration time. Currently, the Pointer technique uses linear simplex, sequential quadratic programming (SQP), downhill simplex, and genetic algorithms. Generally, three optimization technique options need to be set for the Pointer Automatic Optimizer: Maximum Allowable Job Time, Average Analysis Time, and Topography Type. Maximum Allowable Job Time defines the maximum duration for which the optimization process is allowed to run. Average Analysis Time specifies the typical time required for each analysis step during the optimization. Topography Type determines the type of landscape or terrain being considered in the optimization. This process is been illustrated in Figure 7.

The inputs to the process include the design variables, constraints, and the search objective, in addition to the total time available for the search and any previous experience related to the selection and proper configuration of the optimizers. The Pointer control algorithm adjusts the optimizer settings in such a way that either: (1) The best answer is found in the shortest possible time. In this scenario, the optimizers are configured to maximize the

Table 2. Mechanical and thermal properties of GH4099 high-temperature alloy.

Temperature °C	Elastic modulus GPa	Poisson ratio	Thermal expansion coefficient 1×10^{-6}	Density kg/m^3
20	210	0.37	/	8470
400	195	0.36	13.5	
700	167	0.3	14.7	
800	147	0.33	15.1	
1000	121	0.36	17.4	

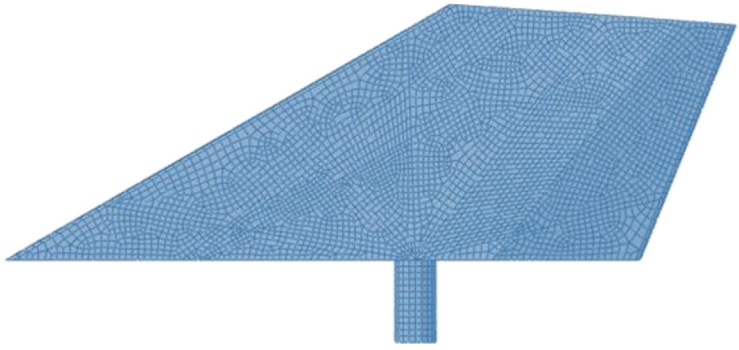

Fig. 8. Finite element model.

Table 3. Responses of the initial rudder.

	1st-order frequency (Hz)	Displacement(mm)					Mass (kg)
		U_{p1}	U_{p2}	U_{p3}	U_{p4}	U_{max}	
Baseline structure responses	141.24	0.71	2.08	3.02	0.50	3.58	4.51

rate of improvement of the objective function from a single starting position; or (2) The most experience is acquired. In this case, the optimizer settings are chosen to achieve the highest optimizer robustness within a given optimization time. Robustness is defined as the mean harmonic error of the best objective function (ever found) normalized by the local optimum across a set of random starting vectors. This approach is an order of magnitude slower than simply finding the best answer. However, the experience gained will enable you to solve similar classes of problems in the shortest possible time. These two strategies switch automatically based on the optimization progress within the same optimization process.

The Pointer control algorithm in the Isight2017 platform has been utilized for the optimization problems presented in this paper. The Maximum Allowable Job Time, Average Analysis Time, and Topography Type have been set to 24 hours, 30 seconds, and non-linear, respectively, based on optimization and simulation tests.

4 Discussion of parametric effects

4.1 Response analysis of initial rudder structure

The reference rudder and its internal structure are similar to those shown in Figure 4. The structure weight is $M = 4.505$ kg, and its geometric dimensions are as described in Section 2.1. In the initial design, the design variables are $X = [45,15,15,15,5,15,5]$, corresponding to the structural geometric dimensions $[t_1,\ t_2,\ t_3,\ t_4,\ t_5,\ t_6] = [5,2,2,2,1,2]$ (mm), and the number of radial ribs is $n_{rb} = 5$.

The material of the rudder structure is GH4099 high-temperature alloy, chosen to withstand the highest anticipated service temperature environment. The main mechanical and thermal properties are summarized in Table 2.

The rudder body is subjected to unilateral pressure, and thermal loads are defined as a temperature field. The amplitude of the pressure load is 0.15 MPa, and the amplitude of the temperature field is 600 °C. At the circumferential surface of the rudder shaft position, the degrees of freedom in three dimensions are constrained. To ensure accurate calculations for thin-walled structures, all components of the rudder structure are modeled using four-node reduced integration shell elements (S4R), as shown in Figure 8. These elements are suitable for four-node doubly curved thin or thick shells and are characterized by reduced integration, hourglass control, and finite membranes.

The results obtained from the analysis are summarized in Table 3 and Figure 9. The output includes the displacement of points $p_1 \sim p_4$, maximum displacement U_{max} of the rudder, first-order frequency, and mass M of the initial structure. The maximum deformation, which occurs at the skin position, is 3.583 mm. The maximum Mises stress is 683 MPa, which is less than the maximum

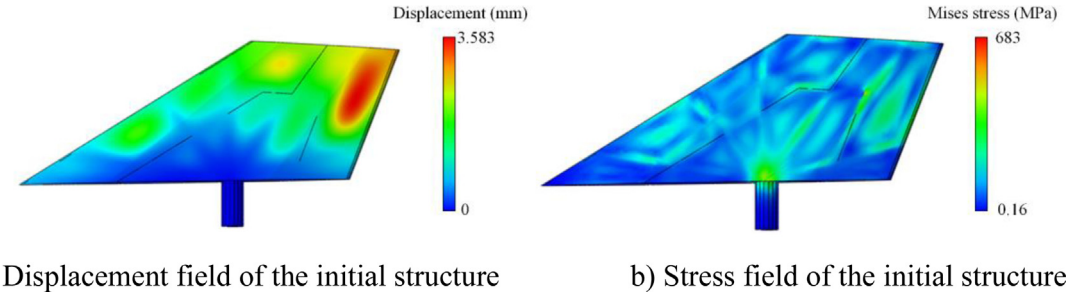

a) Displacement field of the initial structure b) Stress field of the initial structure

Fig. 9. Displacement and stress fields of the initial structure.

allowable stress of the material. The first-order frequency is 141.2 Hz. This initial rudder structure, although not optimized through formal methods, has been obtained after multiple iterations of design, simulation, redesign, and re-simulation. Consequently, it already represents a superior structure compared to that obtained through manual iteration, supported by extensive ground testing. Therefore, its use as the initial structure for optimization analysis can help illustrate the benefits achievable through optimization and facilitate an in-depth examination of the structural parameters under different temperature fields.

Following the analysis of the aforementioned results, the criteria for optimizing the rudder structure are established as follows: (1) The structural weight should not surpass that of the reference rudder structure; (2) The reference frequency should not be lower than that of the reference rudder structure; (3) In consideration of the small absolute value of the maximum deformation, the maximum deformation threshold is allowed to be appropriately increased, but it should not exceed 1% of L_x (Fig. 1).

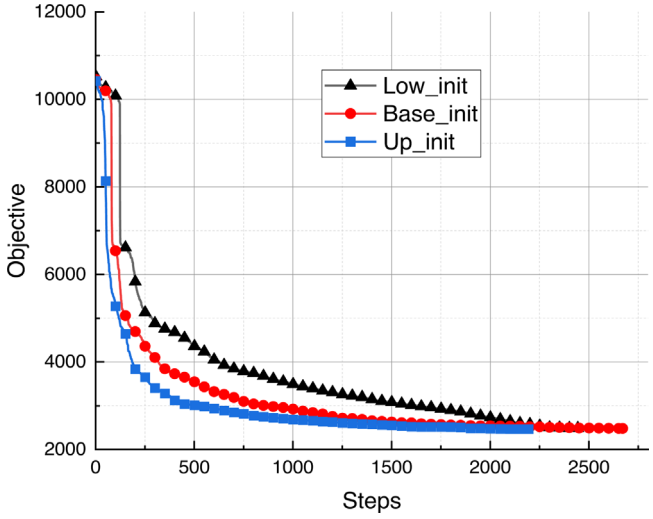

Fig. 10. Iteration history of the objective function.

4.2 Optimization of rudder structure and convergence consistency verification

This section focuses on the optimization of the rudder structure and the verification of convergence consistency with different initial values. These optimization design problems essentially follow the principles of stiffness design and strength verification in structural design. According to the usage requirements, the objective function is designed to include the elastic strain energy, maximum deformation, and structural weight of the rudder. A constraint is introduced to ensure that the first-order frequency of the rudder structure is not less than 141 Hz, which is the first-order natural frequency of the initial rudder structure. The chosen optimization method has been described in Section 3.2. The force load is consistent with that of the initial rudder structure model, consisting of a unilateral skin pressure load. Similarly, the thermal load involves a uniform temperature field, ranging from room temperature to 600 °C.

In the calculation example described herein, equal weight coefficients are assigned to all components of the multi-objective optimization formula, i.e., λ_1=λ_2 = λ_3 = 1. Moreover, to verify the insensitivity of initial values in the optimization framework, three groups of optimization calculations are performed, named Low_init, Base_init, Up_init, based on the lower limit, initial structure variables, and upper limit as initial values for the optimization, respectively.

In Low_init, Base_init, Up_init, the optimal solution is obtained after approximately 72 hours, corresponding to 4504, 4555, and 4503 iterations, respectively, with feasible solutions obtained at 2444, 2671, and 2194 steps, respectively. Because the objective function of infeasible solutions cannot provide meaningful reference, only feasible solutions are presented Figure 10. The horizontal axis presents a high-low ranking of the objective function instead of the typically used number of iterations to facilitate the analysis of the optimal solution. As shown in Table 4, the maximum values of the objective functions of the three examples in the target function are similar, corresponding to the upper boundary of the parameters of the structure. In Table 4, x_3 suddenly drops to 0 for the third example. The results indicate that the values of 0.5 mm or 1.0 mm for t_3 ($t_3 = 0.5 + 0.1 \times x_3$ (mm), $t_3 \in [0.5,\ 5]$) have a limited impact on the objective function and represent two local optima. This also reflects that obtaining the global optimum solution for multi-parameter optimization problems is exceptionally difficult, if not impossible, and one has to settle for a local optimum rather than seeking

Table 4. Optimized parameters corresponding to different examples.

Design variables		x_1	x_2	x_3	x_4	x_5	x_6	x_7
Optimization results	Low_init	18	0	5	0	4	18	5
	Base_init	19	0	5	0	4	17	5
	Up_init	17	0	0	0	4	18	5

Table 5. Responses of the optimized structure.

	1st-order frequency (Hz)	Displacement (mm)					Mass (kg)
		U_{p1}	U_{p2}	U_{p3}	U_{p4}	U_{max}	
Baseline	141.24	0.71	2.08	3.02	0.50	3.58	4.51
Low_init	141.60	0.93	2.24	3.41	0.68	4.46	3.58
Base_init	141.12	0.93	2.29	3.45	0.68	4.47	3.55
Up_init	141.26	0.94	2.25	3.42	0.68	4.50	3.54
Improvement (%)	–0.08	–31.30	–10.15	–14.43	–35.1	–25.59	21.22

the global optimum. Optimization results show that the final optimal solutions are highly consistent, with deviations within 1%.

Tables 4 and 5 presents the optimal solution parameters and key structural responses for the optimal solution, respectively. The optimization parameters and response results obtained in the three examples are consistent with the trend of the objective function. The results of the optimized parameters and structural responses can be found in Table 5. Among the converged and optimized design variables, $x_1 \sim x_5$ decrease to varying degrees, x_6 increases, and x_7 remains unchanged. In other words, x_6 considerably affects the fundamental frequency of the rudder structure. Moreover, x_2 and x_4 reach the lower limit of their design variables, suggesting potential for further reduction. However, because these lower limits are set based on manufacturing constraints, no further reduction is introduced for variables that have reached their lower limits. Specifically, x_2 corresponds to the thickness of the left annular rib, which supports the left part of the rudder and thus must maintain a certain value to preserve its load-bearing capacity. Additionally, x_4 corresponds to the thickness of the outer skin of the rudder. Considering manufacturing constraints and the protective role of the skin on the internal structure, maintaining a minimum skin thickness is necessary.

Table 5 presents optimization examples with three different initial values and comparisons with the structural responses of the initial value structure. It can be observed that, although the weight of the optimized structure has been improved, other indicators have deteriorated to varying degrees. This is due to the fact that, as a multi-objective optimization problem, it is ideal to achieve a decrease in multiple objectives simultaneously, but this is difficult for the problem discussed in this paper.

Figure 11 takes the Base_init case as an example and presents the variation curve of the objective function for the improved optimization results. It can be seen that the objective function has been significantly improved, which demonstrates the effectiveness of the optimization. At the same time, it reflects that for different requirements, different optimization formulations need to be constructed. For example, if maximum deformation is of greater concern, the optimization formulation should be further refined by incorporating key point displacements as constraints.

4.3 Effect of multi-objective weight coefficients

To evaluate the influence of the weight coefficients on the optimized result, this analysis focuses on the effect of the weight coefficients in the multi-objective function on the response of the optimized structure.

First, the optimization results are analyzed when λ_1 is set to 0, 0.2, 0.4, 0.6, 0.8, and 1.0, while values of λ_2 and λ_3 remain constant at 1.0.

Figures 12 and 13 present the impact of coefficient λ_1 on the weight and maximum displacement of the optimized rudder structure, as well as the converged value of the objective function. Figure 12 demonstrates that as the coefficient λ_1 increases, the trends of the maximum deformation and the structural weight are contrary to each other. With the increase of coefficient λ_1, the maximum displacement of the optimized rudder structure gradually decreases, while its structural weight correspondingly increases. Figure 13 shows the variation of the converged objective function with respect to coefficient λ_1. It can be observed that as coefficient λ_1 increases, the optimized objective function exhibits an increasing trend. Coefficient λ_1 affects the extent to which the global objective function's structural strain energy participates in normalizing the overall objective function. Therefore, it is difficult to determine this coefficient. If more influencing factors are considered in the future, it is recommended to set the coefficient at 1.0.

Second, the optimization results are analyzed when λ_2 is set to 0, 0.2, 0.4, 0.6, 0.8, and 1.0, while values of λ_1 and λ_3 remain constant at 1.0.

Figure 14 shows that using the structure weight as a sub-objective function significantly influences the optimized structure. Figure 15 shows the variation of the

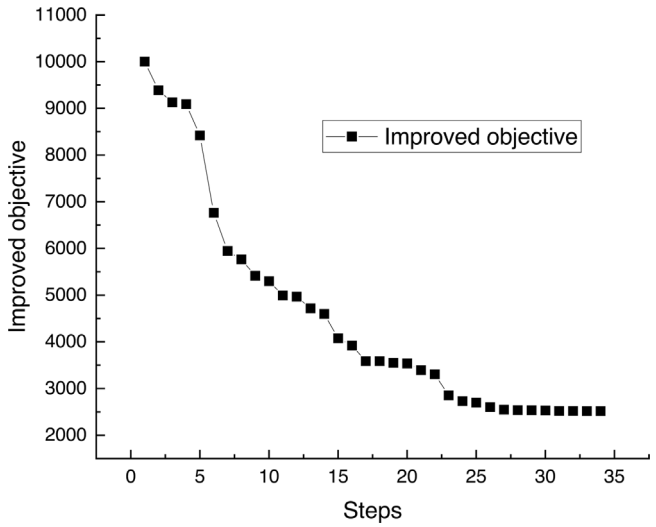

Fig. 11. Improved objective for Base_init optimization example.

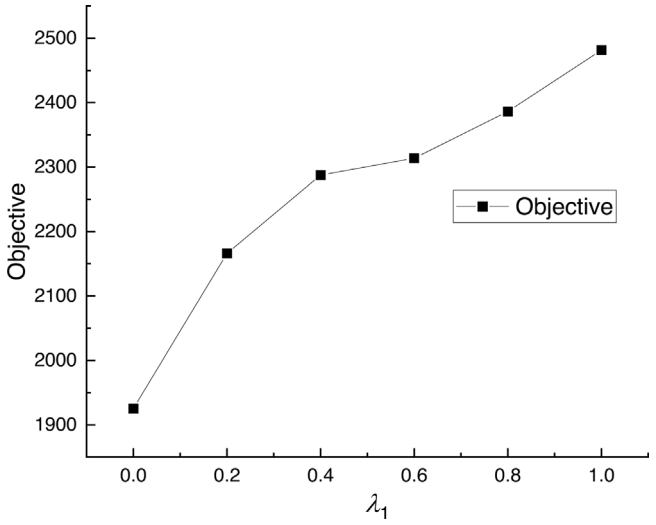

Fig. 13. Effect of coefficient $\boldsymbol{\lambda}_1$ on the converged objective.

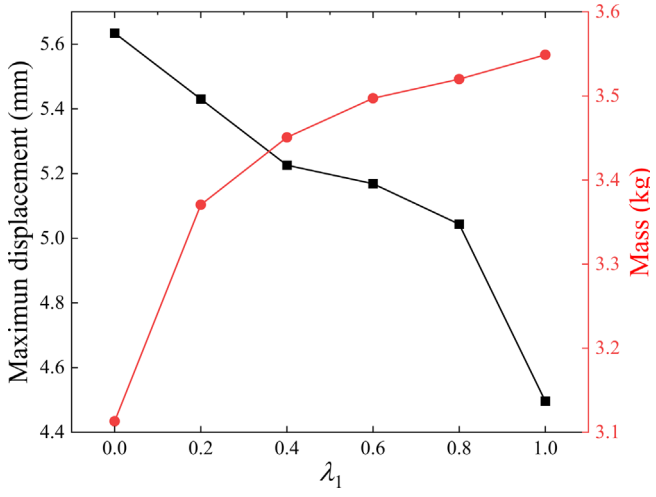

Fig. 12. Effect of $\boldsymbol{\lambda}_1$ on maximum displacement and mass of the optimized structure.

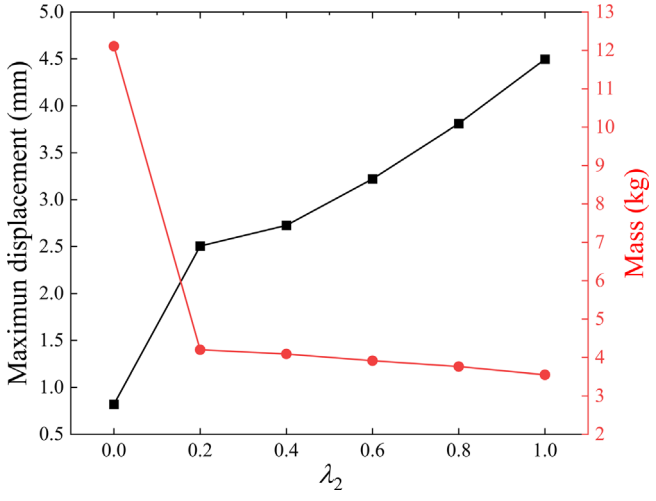

Fig. 14. Effect of $\boldsymbol{\lambda}_2$ on maximum displacement and mass of the optimized structure.

converged objective function with respect to coefficient λ_2. It can be observed that as coefficient λ_2 increases, the optimized objective function exhibits an increasing trend. When $\lambda_2 = 0.2$, the weight of the optimized structure is approximately one-third of that when $\lambda_2 = 0$. As the weight coefficient increases, the weight of the optimized structure gradually decreases, albeit with a diminishing rate of decline. However, the maximum displacement and structural strain energy increases. Therefore, in the multi-objective optimization problem involving the strain energy, structural mass, and maximum displacement, the weight coefficient corresponding to structural mass can be set to 1.0 to reduce the structural weight.

Subsequently, the optimization results are analyzed when λ_3 is set to 0, 0.2, 0.3, 0.4, 0.6, 0.8, and 1.0, while λ_1 and λ_2 remain constant at 1.0.

Figure 16 highlights that using the maximum displacement of the structure as a sub-objective function also significantly influences the optimized structure. Figure 17 shows the variation of the converged objective function with respect to coefficient λ_3. It can be observed that as coefficient λ_3 increases, the optimized objective function exhibits an increasing trend. When $\lambda_3 = 0.4$, the maximum displacement response of the optimized structure is approximately 18% lower than that when $\lambda_3 = 0$. Furthermore, when the coefficient λ_3 is between 0.2 and 0.4, the structural weight increases with the increase of the coefficient, and the maximum displacement decreases with the increase of the coefficient. A supplementary calculation example with a coefficient λ_3 value of 0.3 further verifies this rule. In general, enhancing the weight coefficient results in a diminished displacement response for the optimized structure, demonstrating a monotonic trend in variation. When the weight coefficient is greater than 0.4, further reduction in the structural displacement is limited to within 5%. The influence of the weight coefficient on the weight of the optimized structure is opposite to that of the maximum displacement. This is primarily because the strain energy in the objective function serves to limit the maximum displacement of the structure as well. Therefore,

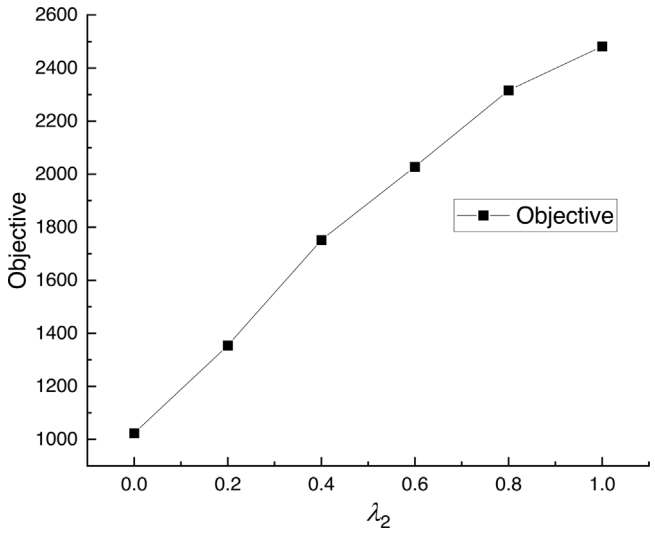

Fig. 15. Effect of coefficient $\boldsymbol{\lambda}_2$ on the converged objective.

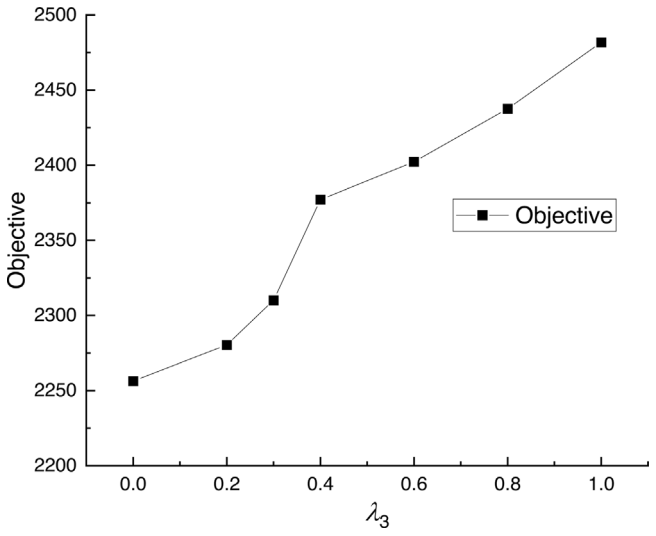

Fig. 17. Effect of coefficient $\boldsymbol{\lambda}_3$ on the converged objective.

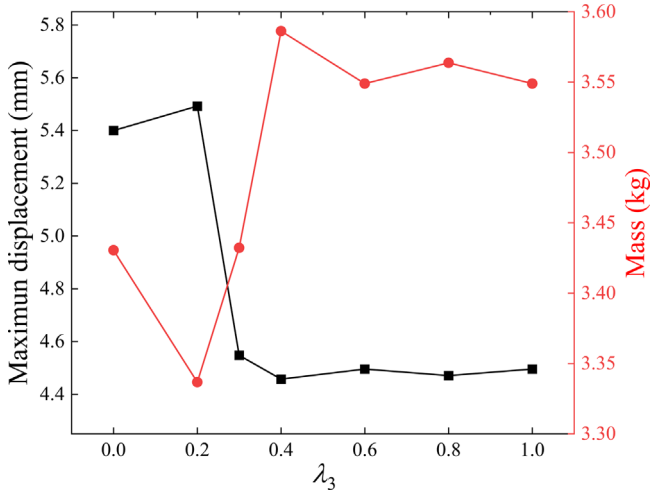

Fig. 16. Effect of $\boldsymbol{\lambda}_3$ on maximum displacement and mass in the optimized results.

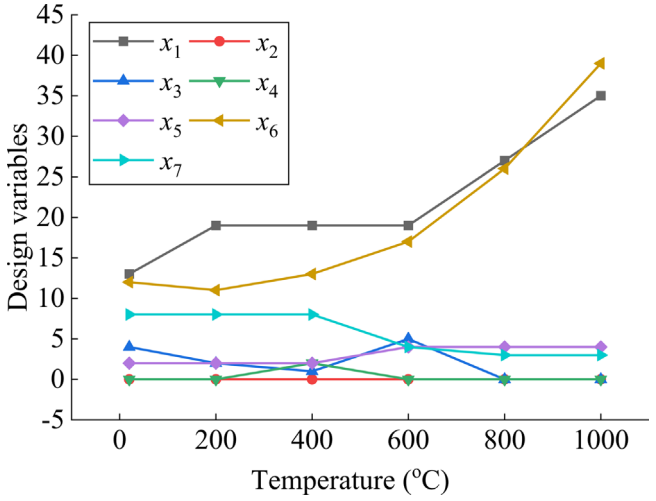

Fig. 18. Optimized design variables for the rudder structure at different temperatures.

in multi-objective optimization problems involving the strain energy, structural mass, and maximum displacement, a weight coefficient value greater than 0.4 can be selected for the maximum displacement to effectively limit the maximum structural deformation. According to data analysis, the recommended value of λ_3 is 0.6 or 1.0.

According to the above analysis, it may be preferable to set $[\lambda_1,\lambda_2,\lambda_3]$ as [1.0, 1.0, 0.6] or [1.0, 1.0, 1.0]. Notably, the aforementioned findings regarding multi-objective weight coefficients are based on the assumption of the same temperature field load. In other situations, findings must be derived according to the specified conditions.

4.4 Influence of temperature on the optimized rudder structure

Building upon the findings from the previous analyses, the effect of temperature fields on the rudder configuration parameters is examined. The material, boundary conditions, and other parameters are identical to those of the initial rudder model. The temperature fields chosen for the optimization design process are 20, 200, 400, 600, 800, and 1000 °C, with the corresponding results labeled T20, T200, T400, T600, T800 and T1000, respectively. According to existing research on multi-objective weight factors, $[\lambda_1,\lambda_2,\lambda_3]$ can be set as [1.0,1.0,0.6] or [1.0,1.0,1.0] to yield feasible optimization results. Further considering that this research pattern has not introduced the influence of temperature, employing [1.0,1.0,1.0] to study the impact of temperature on optimization results can yield more intuitive patterns.

The optimized rudder configuration parameters corresponding to different temperatures and their key responses are presented in Tables 6–8.

Figure 18 shows that the design variables x_1 and x_6, which reflect the thickness values of the base and top plates and thickness of the radial ribs, respectively, increase as the temperature increases. Moreover, the values of x_1 and x_6 in T1000 are three times those in T20, suggesting a strong

Table 6. Optimized parameters corresponding to different cases.

Design variables		x_1	x_2	x_3	x_4	x_5	x_6	x_7
Optimization results	T20	13	0	4	0	2	12	9
	T200	19	0	2	0	2	11	9
	T400	19	0	1	2	2	13	9
	T600	19	0	5	0	4	17	5
	T800	27	0	0	0	4	26	4
	T1000	35	0	0	0	4	39	4

Table 7. Structure responds corresponding to different cases.

		1st order frequency (Hz)	Displacement (mm)					Mass (kg)	Objective
			U_{p1}	U_{p2}	U_{p3}	U_{p4}	U_{max}		
Values	T20	141.51	0.99	1.62	2.84	0.61	3.03	3.28	2097.33
	T200	141.03	0.96	1.70	2.94	0.60	3.15	3.33	2139.53
	T400	141.13	0.97	1.62	2.88	0.59	3.14	3.49	2219.93
	T600	141.12	0.93	2.29	3.45	0.68	4.50	3.55	2481.73
	T800	141.37	1.04	2.31	3.59	0.74	4.96	3.93	2723.68
	T1000	141.21	1.08	2.09	3.57	0.75	5.45	4.66	3201.86

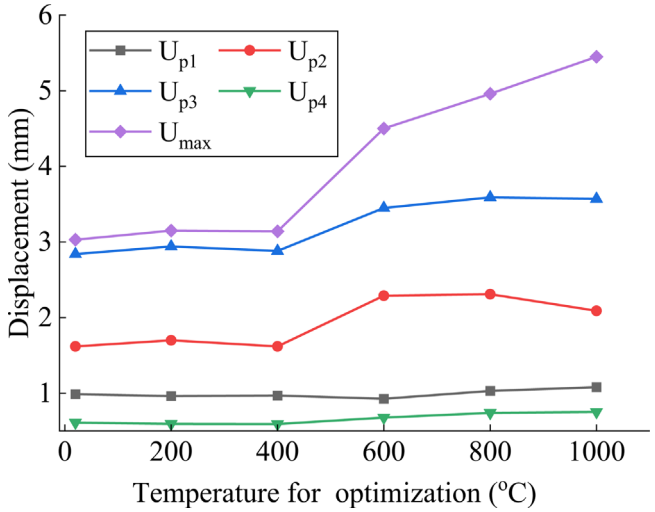

Fig. 19. Displacement response of key points corresponding to the optimized solution under different temperatures.

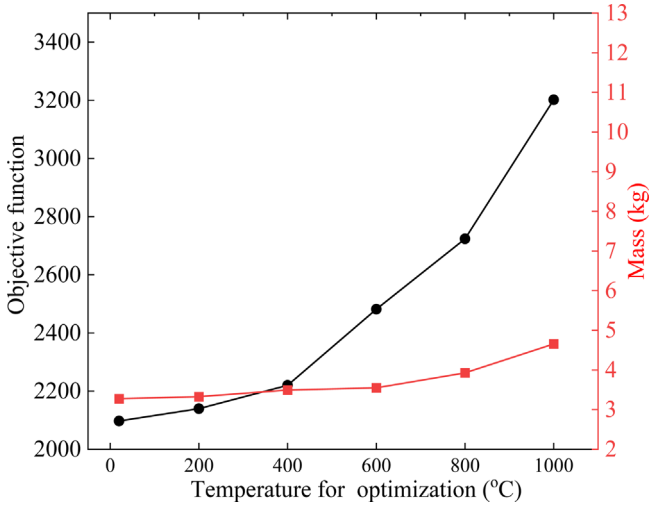

Fig. 20. Objective and mass corresponding to the optimized solution under different temperatures.

correlation with the constraint indicators and objective function. Design variables $x_2 \sim x_4$, which reflect the thickness of the circumferential ribs, converge to the specified lower limit as the temperature rises, indicating a weaker correlation with the objective function. However, to ensure manufacturing processibility and mitigate local deformation, these parameters are not reduced further. Parameter x_5, reflecting the skin thickness, exhibits a step-change characteristic, with T600 serving as the boundary. In general, structures that are considerably influenced by temperature tend to use thicker skin structures. However, owing to the large area covered by the skin, increasing the skin thickness can substantially increase the structural weight. Once converged parameter is reached, no further increase is observed. Parameter x_7, reflecting the number of radial stiffening ribs, exhibits an approximate step-down trend with increasing temperature. Combined with the observed trends of parameter x_6, which pertains to the thickness of the radial stiffening ribs, it is evident that a temperature rise results in a decrease in the number of ribs and increase in the thickness of individual ribs.

In terms of the optimized structural response (Figs. 19 and 20), both the displacement at the four corners of the rudder and the maximum displacement tend to worsen as

Table 8. Optimized structures and responses corresponding to different cases.

Cases	Optimization result		
	Inner structure	Stress field	Displacement field
T20	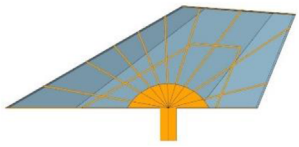	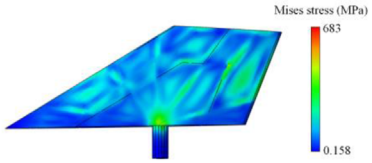	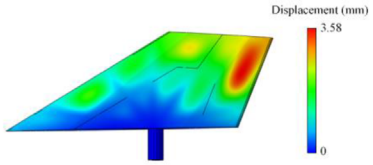
T200	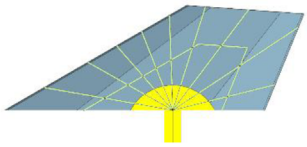	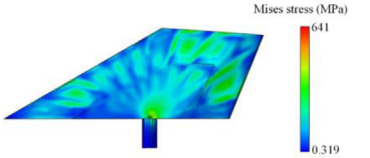	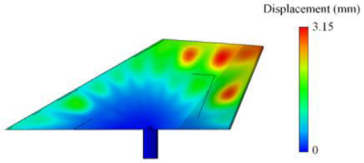
T400	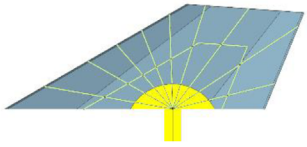	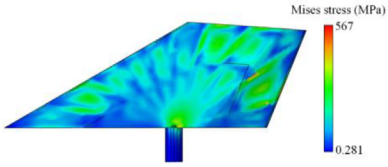	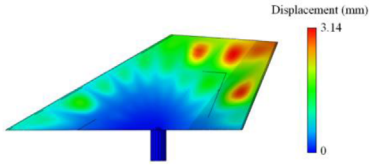
T600	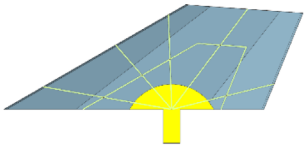	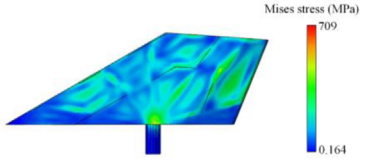	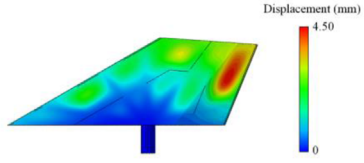
T800	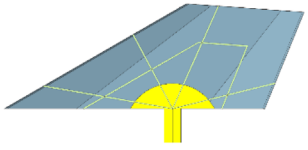	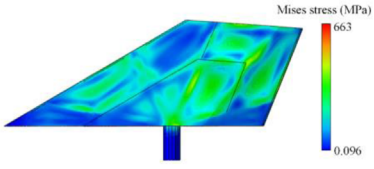	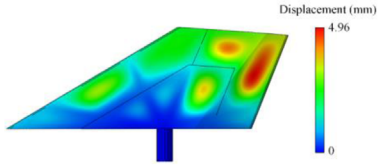
T1000	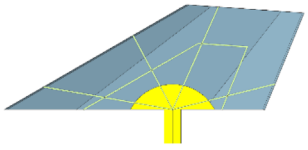	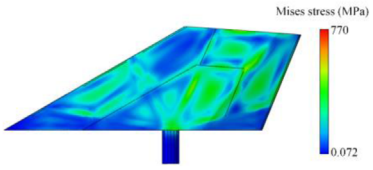	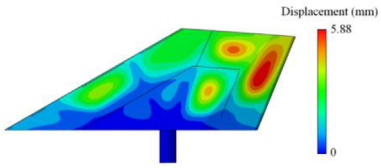

the temperature increases. The most significant change is observed at 1000 °C, where the maximum displacement response reaches 5.45 mm, two times that at room temperature. However, all displacement responses remain within the acceptable range (not exceed 1% of L_x).

Although the structural weight is one of the multiple objective functions, in T20, under equivalent load conditions, a further weight reduction of 21.22% is achieved compared to the initial structure, which already meets the design criteria. However, as the temperature rises, while s maintaining the equivalent frequency constraints, the structural weight increases nonlinearly: a higher temperature results in a higher rate of increase in the structural weight. Moreover, as the temperature rises, the comprehensive objective function response increases in a nonlinear manner, meaning that the objective function response grows more rapidly at higher temperatures.

5 Conclusion

This study focuses on the lightweight optimization design of rudder structures under thermo-mechanical loads. The main research conclusions are as follows:

- A parametric modeling strategy driven by script programs has been set up to construct a parametric model for the co-optimization design of the number and size parameters of reinforcing ribs. To satisfy the multi-objective optimization design requirements, an optimization model based on the compromise programming optimization algorithm is established, facilitating the optimization design of the rudder stiffener configuration and structural parameters. Numerical examples show that the rudder parametric process and model derived from the classical stiffening rib configuration can meet actual engineering needs. Under identical thermo-mechanical loads, the optimized rudder structure achieves a weight reduction of 21.22%. The methodology employed and the research approach can serve as a reference for other multi-objective optimization problems.
- Additionally, this study explores the influence of weight coefficients in multi-objective optimization on the optimized results and analyzes the variation patterns of the optimized load-bearing form and parameters of the rudder structure under varying temperatures. The results indicate that in service conditions involving temperatures up to 600 °C, the changes in structural parameters are minimal. As the maximum service temperature increases beyond 600 °C, indicators such as the maximum deformation and structural weight tend to worsen. This conclusion is based on the corresponding decrease in the elastic modulus and tensile strength of the high-temperature alloy material used in the research with the increase in temperature. For other materials and loads, targeted analysis and optimization research need to be conducted again.
- In the future, models for multidisciplinary optimization of rudder structures, considering more design variables describing topological changes and more complex working conditions, will be studied. Additionally, experimental verification work will be considered.

Acknowledgments

The authors wish to express their appreciation to the reviewers for their helpful suggestions which greatly improved the presentation of this paper.

Funding

This research was funded by the National Key Research and Development Program of China (2020YFB1709405, 2020YFB1709400), the National Natural Science Foundation of China (U1906233, 12272077).

Conflicts of interest

The authors have nothing to disclose.

Data availability statement

The data that support the findings of this study are available from the corresponding author upon reasonable request.

Author contribution statement

Conceptualization, Guanghui Shi, Ran Tao, Wenhua Wu; Methodology, Guanghui Shi, Xiaopeng Zhang; Data Curation, Guiqiang Guo, Ye Lin; Formal Analysis, Guanghui Shi, Xiaopeng Zhang, Yuhao Bao; Writing-Original Draft Preparation, Guanghui Shi, Yuhao Bao; Writing-Review Editing, Guanghui Shi, Ran Tao, Xiaopeng Zhang. All authors contributed to the study conception and design. All authors read and approved the final manuscript.

References

[1] B.W. Li, P. Jin, J. Chen, Aeroelastic tailoring of composite rudder skin considering variable angle tow laminates by a hybrid backtracking search-jaya-sine cosine algorithm, Mech. Adv. Mater. Struc. **1**, 1–14 (2022)
[2] W.R. Wang, Z.G. Wang, S. Wang, H. Deng, H.L. Li, Ablation behavior of rudder wing structure in hypersonic environment, J. Aerosp. Eng. **36**, 04023026 (2023)
[3] L.W. Mott, The Development of the Rudder: A Technological Tale (Texas A&M University Press, USA, 1997)
[4] W.P. Zhang, F.G. Li, J.C. Ma, X.S. Ning, S.L. Sun, Y.L. Hu, Fluid-structure interaction analysis of the rudder vibrations in propeller wake, Ocean Eng. **265**, 112673 (2022)
[5] W.P. Zhang, X.S. Ning, F.G. Li, H. Guo, S.L. Sun, Vibrations of simplified rudder induced by propeller wake, Phys. Fluids **33**, 083618 (2021)
[6] S.G. Parafes, I.K. Turkin, On one approach to design of the rudder-drive system taking into account the aeroelastic stability requirements, Russ. Aeronaut. **63**, 75–82 (2020)
[7] C. Meng, K.H. Yuan, H.B. He, Static aeroelastic effects on rudder efficiency of flying wing aircraft, in Proceedings of 3rd International Conference on Unmanned Systems, Harbin, China (2020), pp. 727–732
[8] R.T. Haftka, Optimization of flexible wing structures subject to strength and induced drag constraints, AIAA J. **15**, 1101–1106 (1977)
[9] S. Grihon, L. Krog, D. Bassir, Numerical optimization applied to structure sizing at AIRBUS: a multi-step process, Int. J. Simul. Multidisci. Des. Optim. **3**, 432–442 (2009)
[10] N. Aage, E. Andreassen, B.S. Lazarov, O. Sigmund, Gigavoxel computational morphogenesis for structural design, Nature **550**, 84–86 (2017)
[11] A. Benaouali, S. Kachel, Multidisciplinary design optimization of aircraft wing using commercial software integration, Aerosp. Sci. Technol. **92**, 766–776 (2019)
[12] A.J. De-wit, W.F. Lammen, W.J. Vankan, H. Timmermans, T. Van-der-laan, P.D. Ciampa, Aircraft rudder optimization – a multi-level and knowledge-enabled approach, Prog. Aerosp. Sci. **119**, 100650 (2020)
[13] D. Bushnell, C. Rankin, Optimum design of stiffened panels with substiffeners, in 46th AIAA/ASME/ASCE/AHS/ASC Structures, Structural Dynamics and Materials Conference, Austin, USA (2005), pp. 1932

[14] P. Hao, B. Wang, G. Li, Z. Meng, K. Tian, X.H. Tang, Hybrid optimization of hierarchical stiffened shells based on smeared stiffener method and finite element method, Thin Wall. Struct. **82**, 46–54 (2014)
[15] B. Wang, P. Hao, G. Li, K. Tian, K.F. Du, X.J. Wang, X. Zhang, X.H. Tang, Two-stage size-layout optimization of axially compressed stiffened panels, Struct. Multidiscipl. Optim. **50**, 313–327 (2014)
[16] D. Bojczuk, W. Szteleblak, Optimization of layout and shape of stiffeners in 2d structures, Comput. Struct. **86**, 1436–1446 (2008)
[17] J.H. Oh, Y.G. Kim, Optimum bolted joints for hybrid composite materials, Compos. Struct. **38**, 329–341 (1997)
[18] K.J. Jadee, A.R. Othman, Fiber reinforced composite structure with bolted joint − a review, Key Eng. Mater. **471**, 939–944 (2011)
[19] H.H. Gao, J.H. Zhu, W.H. Zhang, Y. Zhou, An improved adaptive constraint aggregation for integrated layout and topology optimization, Comput. Methods Appl. Mech. Eng. **289**, 387–408 (2015)
[20] L. Xia, J.H. Zhu, W.H. Zhang, A superelement formulation for the efficient layout design of complex multi-component system, Struct. Multidiscipl. Optim. **45**, 643–655 (2012)
[21] L. Xia, J.H. Zhu, W.H. Zhang, Sensitivity analysis with the modified heaviside function for the optimal layout design of multi-component systems, Comput. Methods Appl. Mech. Eng. **241**, 142–154 (2012)
[22] D.L. Quan, G.H. Shi, C.Q. Guan, J. Wang, J.H. Luo, F. Song, B. Wang, J.H. Zhu, W.H. Zhang, Applications and challenges of structural optimization in high-speed aerocraft, Mech. Eng. **41**, 373–381 (2019)
[23] J.H. Zhu, Y.B. Zhao, W.H. Zhang, X.J. Guo, T. Gao, J. Kong, G.H. Shi, Y.J. Xu, D.L. Quan, Bio-inspired feature-driven topology optimization for rudder structure design, Eng. Sci. **5**, 46–55 (2018)
[24] C. Wang, J.H. Zhu, M.Q. Wu, J. Hou, H. Zhou, L. Meng, C.Y. Li, W.H. Zhang, Multi-scale design and optimization for solid-lattice hybrid structures and their application to aerospace vehicle components, Chin. J. Aeronaut. **34**, 386–398 (2021)
[25] L.L. Song, T. Gao, L. Tang, X.X. Du, J.H. Zhu, Y. Lin, G.H. Shi, H. Liu, G.N. Zhou, W.H. Zhang, An all-movable rudder designed by thermo-elastic topology optimization and manufactured by additive manufacturing, Comput. Struct. **243**, 106405 (2021)
[26] M. Zhou, R. Fleury, Y.K. Shyy, H. Thomas, J. Brennan, Progress in topology optimization with manufacturing constraints, in 9th AIAA/ISSMO Symposium on multidisciplinary analysis and optimization, Atlanta, USA (2002), pp. 5614
[27] L. Harzheim, G. Gerhard, A review of optimization of cast parts using topology optimization: ii-topology optimization with manufacturing constraints, Struct. Multidiscipl. Optim. **31**, 388–399 (2005)
[28] Q. Xia, T.L. Shi, M.Y. Wang, S.Y. Liu, A level set based method for the optimization of cast part, Struct. Multidiscipl. Optim. **41**, 735–747 (2010)
[29] S.S. Rao, Optimization of airplane wing structures under landing loads, Comput. Struct. **19**, 849–863 (1984)
[30] L. Li, J.Q. Bai, T.B. Guo, X.L. He, Z.Y. Fu, Aerodynamic design of the supersonic aircraft wing-shape and wing-twist optimization, Int. J. Aeronaut. Space Sci. **19**, 340–353 (2018)
[31] Z. Qun, Y.L. Ding, H.B. Jin, A layout optimization method of composite wing structures based on carrying efficiency criterion, Chin. J. Aeronaut. **24**, 425–433 (2011)
[32] T. Long, Y.F. Wu, Z. Wang, Y.F. Tang, D. Wu, Y. Yu, Efficient aero-structure coupled wing optimization using decomposition and adaptive metamodeling techniques, Aerosp. Sci. Technol. **95**, 105496 (2019)
[33] Z.D. Hu, J. Qiu, F. Zhang, Fully parametric optimization designs of wing components, Int. J. Aerosp. Eng. 2020, 8841623 (2020)
[34] G.H. Shi, C.Q. Guan, D.L. Quan, D.T. Wu, L. Tang, T. Gao, An aerospace bracket designed by thermo-elastic topology optimization and manufactured by additive manufacturing, Chin. J. Aeronaut. **33**, 1252–1259 (2020)
[35] W.L. Ko, L. Gong, Thermostructural analysis of unconventional wing structures of a hyper-x hypersonic flight research vehicle for the Mach 7 mission, Nasa TP-2001–210398 (2001)
[36] J.F. Chen, D.J. Wang, D. Yang, Missile and spacecraft structure analysis and design (Northwest University Press, Xian, 1995)
[37] E.S. Lee, R.J. Li, Fuzzy multiple objective programming and compromise programming with pareto optimum, Fuzzy Sets Syst. **53**, 275–288 (1993)
[38] W.H. Zhang, A compromise programming method using multibounds formulation and dual approach for multicriteria structural optimization, Int. J. Numer. Methods Eng. **58**, 661–678 (2003)
[39] H.X. Qin, Q.D. Yang, Compromise programming approach with grey weight factor for structural topology optimization under multiple load conditions, Chin. Quart. Mech. **39**, 280 (2018)
[40] Z. Luo, J. Yang, L. Chen, A new procedure for aerodynamic missile designs using topological optimization approach of continuum structures, Aerosp. Sci. Technol. **10**, 364–373 (2006)
[41] W.C. Fan, Z.M. Xu, B. Wu, Y.S. He, Z.F. Zhang, Structural multi-objective topology optimization and application based on the criteria importance through intercriteria correlation method, Eng. Optim. **54**, 830–846 (2022)
[42] M.R. Sharifi, S. Akbarifard, K. Qaderi, M.R. Madadi. A new optimization algorithm to solve multi-objective problems, Sci Rep. **11**, 20326 (2021)
[43] W.J. Fan, Z. Fan, R. Su. Research on multi-objective topology optimization on bus chassis frame, Chin. J. Mech. Eng. **19**, 1505–1508 (2008)
[44] D.J. Munk, T. Kipouros, G.A. Vio et al., Multiobjective and multi-physics topology optimization using an updated smart normal constraint bi-directional evolutionary structural optimization method, Struct Multidisc Optim. **57**, 665–688 (2018)
[45] A.V. Velden, D. Kokan, The synaps pointer optimization engine, International design engineering technical conferences and computers and information in engineering conference, Montreal, France, 2002, pp. 159–165
[46] Y.T. Zhu, M. Datar, K. Addepalli, R. Natalie, Optimization of front wheel drive engine mounting system for third order shudder improvement, SAE Int. J. Commer. Veh. **10**, 1–7 (2017)

[47] P. Piperni, A. DeBlois, R. Henderson, Development of a multilevel multidisciplinary-optimization capability for an industrial environment, AIAA J. **51**, 2335–2352 (2013)

[48] J. Yang, F. Wang, Y. Lu, Design of a bistable artificial venus flytrap actuated by low pressure with larger capture range and faster responsiveness, Biomimetics **8**, 181 (2023)

Cite this article as: G. Shi, Y. Bao, W. Wu, G. Guo, Y. Lin, X. Zhang, R. Tao, Parametric-modeling-based multi-objective thermoelastic optimization of rudder structures, Mechanics & Industry 26, 9 (2025), https://doi.org/10.1051/meca/2025002